

Sparse Mamba Decoder for Quantum Error Correction: Efficient Defect-Centric Processing of Surface Code Syndromes

Samira Sayedsalehi*, Nader Bagherzadeh, Maxim Shcherbakov, and Jean-Luc Gaudiot

*Department of Electrical Engineering and Computer Science
University of California, Irvine, CA 92697, USA*

Abstract

Quantum error correction (QEC) is essential for building fault-tolerant quantum computers, requiring decoders that are simultaneously accurate, fast, and scalable. Most state-of-the-art neural decoders achieve high accuracy but process the full dense syndrome array of size $\mathcal{O}(d^2R)$ regardless of the actual error rate, where d is the code distance and R is the number of measurement rounds. At physically relevant error rates ($p \approx 0.1\%$), fewer than 5% of syndrome entries contain active detection events—yet existing decoders process the entire syndrome volume. We introduce the Sparse Mamba Decoder (SMD), a defect-centric neural decoder that processes only the k active detection events using a 13-dimensional feature representation per defect and a Mamba state-space backbone, achieving $\mathcal{O}(k)$ complexity. Across depolarizing, uniform circuit-level, S11000, and Google Sycamore experimental benchmarks, SMD reduces the MWPM logical error rate by up to 49% at $d \leq 5$ under S11000 noise, runs 95–467 \times faster than the Tesseract near-MLD decoder and 232–463 \times faster than Belief Matching, and maintains nearly constant latency (24–57 μs) across $d = 3$ –9 under uniform circuit-level noise. On the Sycamore experimental dataset, the SMD ensemble matches or slightly surpasses the dense Mamba decoder of Lee et al. All results are obtained on commodity NVIDIA GPUs with 7.5–16M parameters, without specialized accelerators.

1 Introduction

Fault-tolerant quantum computing requires logical error rates far below those achievable with physical qubits, necessitating quantum error correction (QEC) codes that encode logical information redundantly across many physical qubits [1, 2]. The surface code [3, 4] is the leading candidate for near-term implementation due to its high threshold error rate and local stabilizer structure, and continues to see active research in code design [5] and decoder development. However, the practical utility of any QEC code depends critically on the *decoder*—the classical algorithm that infers logical errors from noisy stabilizer measurements.

An ideal decoder must satisfy three competing requirements simultaneously: *accuracy* (approaching the maximum-likelihood estimate), *speed* (keeping pace with the quantum hardware cycle time, typically $\sim 1 \mu\text{s}$ for superconducting qubits [6]), and *scalability* (maintaining performance as code distance increases). In practice, existing decoders make tradeoffs among these three axes, and achieving all three simultaneously—particularly at the code distances required for fault tolerance—remains an open challenge.

Minimum-Weight Perfect Matching (MWPM) [7, 8] is fast and scalable but suboptimal, as it does not account for correlated errors. The Tesseract decoder [9] achieves near-optimal accuracy through beam search over the detector error model but requires millisecond-scale computation. AlphaQubit [10] introduced a recurrent-transformer architecture that outperforms all matching-based decoders on experimental data, but its $\mathcal{O}(d^4)$ per-round attention complexity

*Corresponding author. Email: ssayedsa@uci.edu

makes real-time decoding impractical at large distances. AlphaQubit 2 [11] addresses this with a redesigned architecture achieving $\mathcal{O}(d^2)$ per-round scaling and real-time decoding up to distance 11, but requires specialized Trillium TPU hardware [12]. Lee et al. [13] proposed replacing the transformer with a Mamba state-space model [14], reducing the complexity to $\mathcal{O}(d^2)$ while maintaining accuracy on consumer GPUs.

Despite these advances, most existing neural decoders share a fundamental inefficiency: they process the *full* syndrome array of size $d^2 \times R$ at every decoding step, regardless of how many errors actually occurred. The graph-neural-network decoder of Lange et al. [15] operates on detection events but requires explicit graph construction and message-passing operations that are less GPU-friendly than pure sequence processing. At a physical error rate of $p = 10^{-3}$ under SI1000 noise, only a few percent of stabilizer measurements fire—we measure detection-event densities of 2.8–3.2% across $d = 3$ –7 (Table 10). Yet existing decoders process every entry of the syndrome volume, analogous to running a dense matrix multiplication on a 97%-sparse matrix.

In this work, we introduce the Sparse Mamba Decoder (SMD), which fundamentally changes the input representation from dense syndrome arrays to sparse defect sequences. Each active detection event is represented by a 13-dimensional feature vector encoding spatial coordinates on the rotated lattice, stabilizer type (X or Z), spatial and temporal neighborhood connectivity flags, normalized distances to the logical boundaries, and a reconstructed stabilizer measurement computed via cumulative XOR of the per-stabilizer detection event history. The resulting variable-length sequences—typically $k \ll d^2 R$ at physically relevant error rates—are processed by a Mamba state-space backbone [14] in linear time without attention. This yields $\mathcal{O}(k)$ complexity, compared to $\mathcal{O}(d^2 R)$ for dense neural decoders and $\mathcal{O}(d^4 R)$ for attention-based methods. Throughout this paper, complexity is reported per decoding task (one logical qubit memory experiment over R rounds); equivalent per-round costs for recurrent decoders are obtained by dividing by R , e.g., $\mathcal{O}(d^2)$ per round for dense Mamba [13] and $\mathcal{O}(d^4)$ per round for AlphaQubit [10].

Our main contributions are:

1. A sparse defect-centric architecture for QEC decoding. SMD processes only active detection events through a Mamba state-space backbone, achieving $\mathcal{O}(k)$ complexity that scales with the number of errors rather than the code size. The 13-dimensional defect features encode the spatial structure and measurement history needed for accurate decoding without explicit 2D convolutions.
2. Strong accuracy across synthetic and experimental benchmarks. Under SI1000 noise at $p = 1.5 \times 10^{-3}$, SMD reduces the MWPM logical error rate by up to 49% at $d \leq 5$ and by 16% at $d = 7$ via a three-checkpoint ensemble, where a Libra-style ensemble of seven perturbed MWPM decoders gives no improvement, isolating the gain to learned correlations. On the Sycamore dataset, the SMD ensemble matches or slightly surpasses the dense Mamba decoder of Lee et al. [13] at both $d = 3$ and $d = 5$, while the single-model SMD remains competitive at $d = 3$ and approaches dense-Mamba performance at $d = 5$.
3. Order-of-magnitude speedups over near-MLD decoders. Under SI1000 noise, SMD runs $95 \times$ – $467 \times$ faster than Tesseract and $232 \times$ – $463 \times$ faster than Belief Matching, with the speedup growing with code distance. Under uniform circuit-level noise, decoding latency is nearly constant (24 – $57 \mu\text{s}$) across $d = 3$ –9, compared to a $773 \times$ increase for Belief Matching over the same range.
4. Commodity-hardware feasibility. All results are obtained on commodity NVIDIA GPUs—an RTX 4090 (24 GB) for the smaller depolarizing and uniform circuit-level models, and a single H200 NVL (141 GB) for the larger SI1000 model—without the specialized Trillium TPUs used by AlphaQubit 2 [11, 12].

2 Background

2.1 Surface Codes and Stabilizer Measurements

The rotated surface code of distance d encodes one logical qubit into d^2 data qubits using a CSS (Calderbank-Shor-Steane) structure of $(d^2 - 1)$ stabilizer measurements arranged in a checkerboard pattern on a two-dimensional lattice [4] (Figure 1). These stabilizers form two independent families: Z -type checks detect X -errors (bit flips) by measuring the Z -parity of adjacent data qubits, while X -type checks detect Z -errors (phase flips) by measuring the X -parity of their neighbors; a Y -error triggers both check types simultaneously, enabling its identification. In a memory experiment, stabilizer measurements are repeated for R rounds, producing a syndrome array of shape $(d^2 - 1) \times R$, with X and Z corrections handled independently.

A *detection event* at stabilizer i and round t is defined as the temporal difference of consecutive measurements:

$$d_{i,t} = s_{i,t} \oplus s_{i,t-1}, \quad (1)$$

where $s_{i,t} \in \{0,1\}$ is the raw measurement outcome and \oplus denotes XOR. In the absence of errors, all detection events are zero; physical errors on data qubits trigger clusters of nearby detection events in space-time.

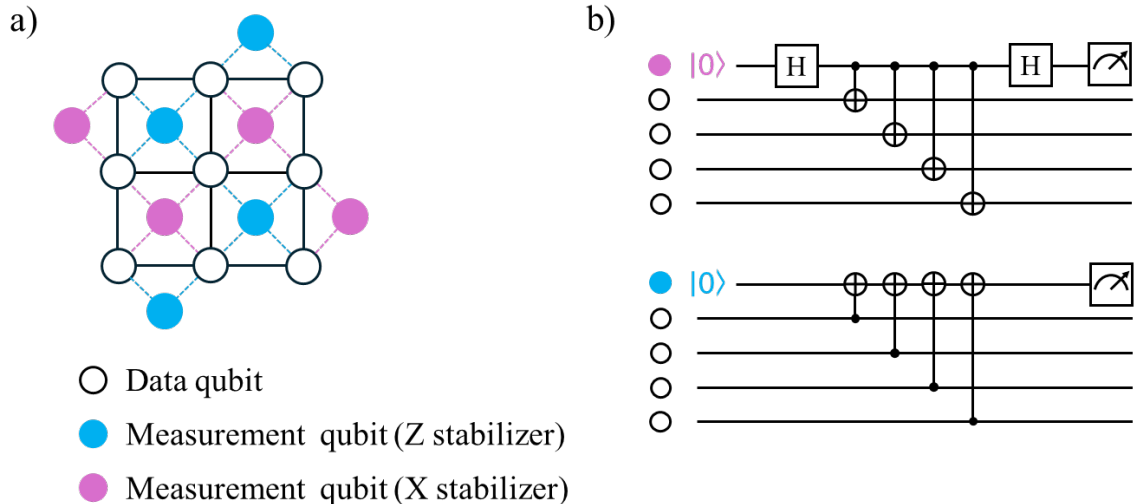


Figure 1: a) Planar layout of a rotated surface code with code distance $d = 3$. White circles represent data qubits, while blue circles \bullet and pink circles \bullet represent Z -type and X -type stabilizer measurement qubits, respectively. b) Circuit representation of the X -type (top) and Z -type (bottom) stabilizer measurements. Open circles (\circ) denote the four data qubits coupled to each measurement qubit.

The decoder's task is to predict the logical observable $\lambda \in \{0,1\}$ from the set of detection events $\{d_{i,t}\}_{i,t}$, determining whether a logical error has occurred.

2.2 The Decoding Problem

Given a syndrome $\sigma = \{d_{i,t}\}$, the optimal decoder predicts the most likely logical observable:

$$\hat{\lambda} = \arg \max_{\lambda \in \{0,1\}} P(\lambda | \sigma), \quad (2)$$

which requires marginalizing over all physical error configurations consistent with the observed syndrome. This decoding problem is NP-hard in general [16]. Practical decoders approximate this inference using matching-based methods (MWPM [7]), tensor-network contraction [17], or learned neural networks [10, 13].

2.3 Related Work

Matching-based decoders reduce the decoding problem to a minimum-weight perfect matching on a graph derived from the detector error model. MWPM [8] and its correlated variants achieve a circuit-level threshold of approximately 0.5–1%, with Sparse Blossom [7] achieving $\mathcal{O}(n^{1.32})$ observed complexity. Union-Find [18] offers near-linear $\mathcal{O}(n\alpha(n))$ complexity at slightly reduced accuracy. Belief Matching [19] combines belief propagation with matching-based decoding and improves accuracy under circuit-level noise, although belief propagation alone can perform poorly on surface codes due to short cycles in the Tanner graph. The Tesseract decoder [9] reaches near-optimal accuracy through beam search over the detector error model, but at millisecond-scale per-shot cost. Recently, ensemble approaches such as Libra [20] have explored combining multiple perturbed matching decoders to close the residual gap to maximum-likelihood decoding. For small codes, contracting the tensor network defined by the syndrome distribution provides a near-optimal but exponentially expensive baseline [17], which we use as a reference on the Sycamore experimental dataset.

Neural decoders learn representations of the syndrome history from data, reducing reliance on explicit error-model priors. AlphaQubit [10] introduced a recurrent-transformer architecture trained on both simulated and experimental data, outperforming matching decoders on the Sycamore quantum processor. Its successor, AlphaQubit 2 [11], includes a compact real-time variant (AQ2-RT) that achieves $< 1 \mu\text{s}/\text{cycle}$ decoding up to distance 11 on Trillium TPUs [12]. Lee et al. [13] replaced the transformer core with a Mamba state-space model [14], reducing complexity from $\mathcal{O}(d^4)$ to $\mathcal{O}(d^2)$ per round while matching transformer accuracy on the Sycamore benchmark with logical error rates of 2.98% at $d=3$ and 3.03% at $d=5$. Lange et al. [15] proposed a graph-neural-network decoder for circuit-level noise, with performance approximately matching MWPM. These dense neural decoders process information proportional to the full syndrome volume $d^2 \times R$, regardless of the actual error rate. In contrast, our Sparse Mamba Decoder processes only the k active detection events, yielding neural-processing cost $\mathcal{O}(k)$ with $k \ll d^2 R$ at physically relevant error rates. Table 3 summarizes the comparison.

3 Method: Sparse Mamba Decoder

A physical Pauli error on a data qubit persists until corrected; left in place, it would cause its adjacent stabilizers to fire every subsequent round, producing a dense “always-on” syndrome. The detection event $d_{i,t} = s_{i,t} \oplus s_{i,t-1}$ converts this persistent state into a sparse spacetime signal: each error contributes detection events only at the *endpoints* of its trajectory in spacetime, where it appears and where it is cancelled. This is the structural reason the syndrome volume is overwhelmingly zero at physical error rates of interest.

For a distance- d surface code with R rounds of stabilizer measurements, the syndrome volume contains $(d^2 - 1) \times R$ entries, but the expected number of active detection events is

$$\mathbb{E}[k] \approx (d^2 - 1) \times R \times \rho(p), \quad (3)$$

where $\rho(p)$ is the detection event density at physical error rate p . At $p = 10^{-3}$ under SI1000 noise, we measure $\rho \approx 0.03$ (Table 10), yielding $k \ll d^2 R$ ($\sim 30\times$ reduction at $d = 7$, $R = 120$). SMD operates on this k -token sparse sequence, not on the full $d^2 R$ volume (Fig. 2a).

We extract the active detection events from the entire syndrome volume and represent each as a 13-dimensional feature vector (Fig. 2b). For a defect at stabilizer i in round t , this vector is

$$\mathbf{f}_{i,t} = \left[\underbrace{x_i, y_i}_{\text{spatial}}, \underbrace{t/R}_{\text{temporal}}, \underbrace{\tau_i}_{\text{type}}, \underbrace{n_1, \dots, n_4}_{\text{spatial nb.}}, \underbrace{n_5, n_6}_{\text{temporal nb.}}, \underbrace{b_Z, b_X}_{\text{boundary}}, \underbrace{m_{i,t}}_{\text{measurement}} \right], \quad (4)$$

where (x_i, y_i) are the normalized stabilizer coordinates on the rotated lattice; t/R is the normalized round index; $\tau_i \in \{0, 1\}$ indicates the stabilizer type (X- or Z-type); n_1, \dots, n_4 are binary

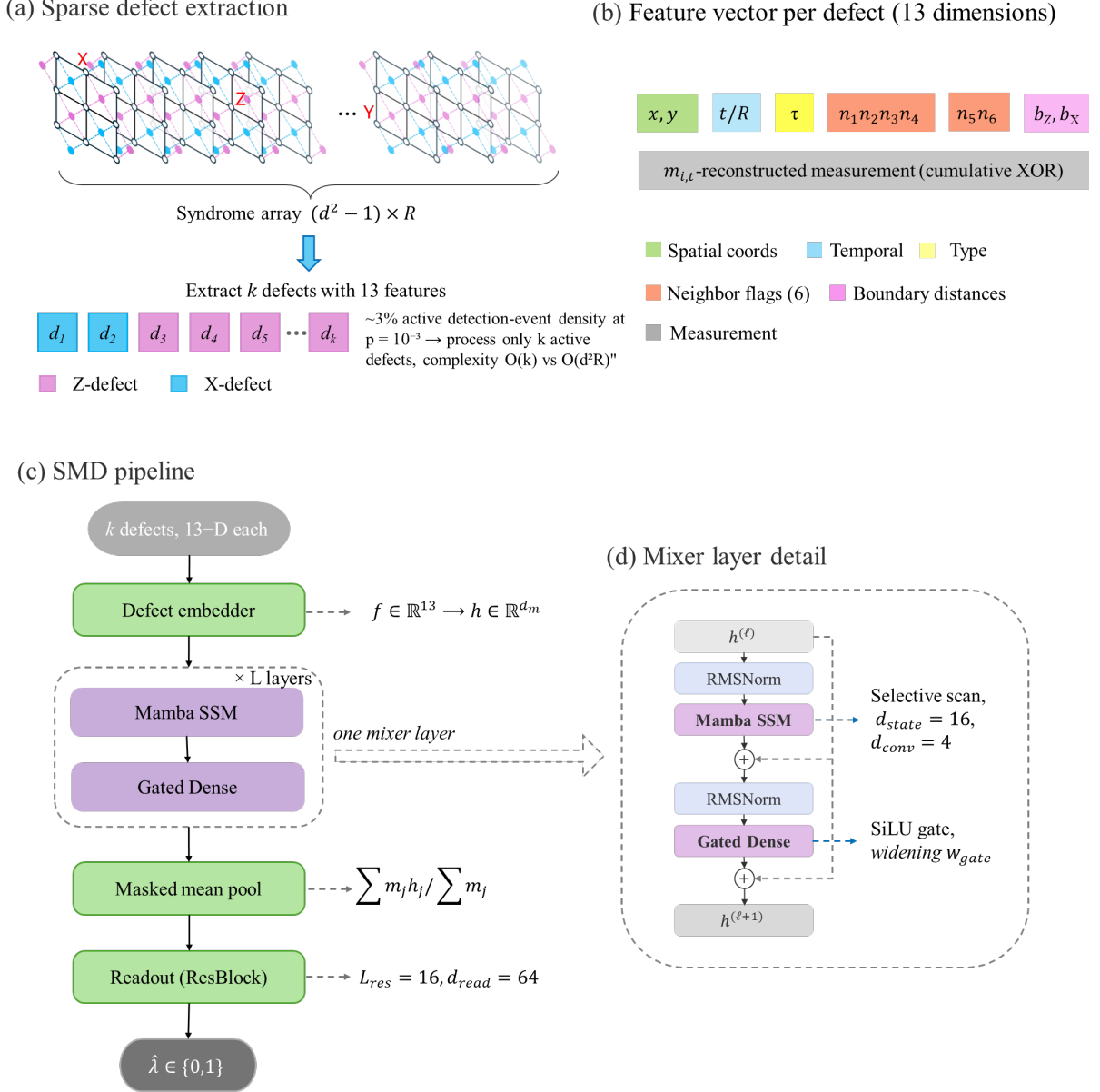


Figure 2: Sparse Mamba Decoder architecture. **(a)** Sparse defect extraction from a $(d^2 - 1) \times R$ syndrome volume to k defect tokens d_1, \dots, d_k ($k \ll d^2 R$ at physically relevant error rates). **(b)** 13-dimensional feature vector per defect: spatial coordinates (x, y) , normalized time t/R , stabilizer type τ , spatial and temporal neighbor flags, boundary distances b_Z, b_X , and the reconstructed measurement $m_{i,t}$ from cumulative XOR. **(c)** Pipeline: per-token embedder $\mathbb{R}^{13} \rightarrow \mathbb{R}^{d_{\text{model}}}$, L mixer layers, masked mean pool, ResBlock readout to logical observable $\hat{\lambda}$. **(d)** One mixer layer: RMSNorm + Mamba selective scan ($d_{\text{state}}=16, d_{\text{conv}}=4$), then RMSNorm + Gated Dense (SiLU gating, widening w_{gate}), both with residual connections.

flags indicating whether each of the four spatial neighbors also fired in round t ; n_5, n_6 are binary flags for the temporal neighbors at rounds $t - 1$ and $t + 1$; b_Z, b_X are normalized distances to the Z and X logical boundaries; and $m_{i,t}$ is the reconstructed measurement, computed as the cumulative XOR of detection events:

$$m_{i,t} = d_{i,1} \oplus d_{i,2} \oplus \dots \oplus d_{i,t} = \bigoplus_{s=1}^t d_{i,s}. \quad (5)$$

The reconstructed measurement $m_{i,t}$ recovers the raw stabilizer measurement outcome (up to the unknown initial state), providing the model with a dual view: the detection event indicates *where errors changed*, while the reconstructed measurement indicates the *current state* of each stabilizer. This dual-input approach was shown to be beneficial by Bausch et al. [10] for dense representations; we adapt it here for sparse defect sequences.

After all R rounds of stabilizer measurement complete, we extract the active defects from the entire syndrome volume in one pass and sort them by time (primary) and stabilizer index (secondary). This produces a single ordered defect sequence of length k . Sequences are padded to a fixed maximum length k_{\max} with a binary mask, yielding a batch representation of shape $(B, k_{\max}, 13)$ with mask (B, k_{\max}) . Critically, defects are processed as a unified sequence: SMD does not advance a hidden state (the internal vector representation $\mathbf{h}^{(\ell)} \in \mathbb{R}^{d_{\text{model}}}$ carrying information through the network) per measurement round. While the one-time dense-to-sparse extraction requires a pass over the syndrome volume (cost $\mathcal{O}(d^2 R)$), all subsequent neural processing scales as $\mathcal{O}(k)$ in the active defect count. Future hardware-integrated implementations could emit detection events directly as a sparse stream, eliminating the dense scan and making the entire pipeline sparse.

3.1 Decoder Architecture

SMD processes the k -token defect sequence in a single forward pass (Fig. 2c):

$$\text{DefectEmbed} \rightarrow L \times \text{MixerLayer} \rightarrow \text{MaskedPool} \rightarrow \text{Readout} \rightarrow \hat{\lambda}. \quad (6)$$

There is no per-round recurrence: a single Mamba stack consumes the entire defect sequence at once.

The defect embedder projects the 13-dimensional feature vector to the model dimension d_{model} through a two-layer MLP with LayerNorm and GELU activation, applied independently and in parallel to each token:

$$\mathbf{h}^{(0)} = \text{LayerNorm}(W_2 \text{GELU}(\text{LayerNorm}(W_1 \mathbf{f} + b_1)) + b_2). \quad (7)$$

Each of the L subsequent mixer layers applies a Mamba selective state-space block [14] followed by a gated dense block, with RMSNorm and residual connections (Fig. 2d):

$$\mathbf{z} = \mathbf{h}^{(\ell)} + \text{Mamba}(\text{RMSNorm}(\mathbf{h}^{(\ell)})), \quad (8)$$

$$\mathbf{h}^{(\ell+1)} = \mathbf{z} + \text{GatedDense}(\text{RMSNorm}(\mathbf{z})), \quad (9)$$

where the GatedDense block consists of two parallel linear projections with SiLU gating:

$$\text{GatedDense}(\mathbf{x}) = W_c(\text{SiLU}(W_a \mathbf{x}) \odot W_b \mathbf{x}). \quad (10)$$

The widening factor w_{gate} controls the intermediate dimension $w_{\text{gate}} \cdot d_{\text{model}}$. The Mamba block uses a selective scan mechanism [14] with state dimension d_{state} and convolution width d_{conv} . The Mamba block mixes information *across* the k tokens of the defect sequence, while the GatedDense block mixes information *within* each token across the d_{model} channels.

In contrast to the dense recurrent decoders of AlphaQubit [10, 11] and Lee et al. [13], our mixer layer contains no explicit spatial-reshape operations: the Syndrome Mixer of Lee et al. additionally requires Scatter-to-2D, dilated 2D convolutions, and Gather-from-2D operations to capture geometric correlations across stabilizers, whereas SMD encodes spatial structure directly in the 13-D feature vector and processes the defect sequence with Mamba alone.

After L mixer layers, we aggregate the variable-length defect representations using masked mean pooling:

$$\bar{\mathbf{h}} = \frac{\sum_j m_j \cdot \mathbf{h}_j^{(L)}}{\sum_j m_j + \epsilon}, \quad (11)$$

where $m_j \in \{0, 1\}$ is the binary mask for position j (1 for real defects, 0 for padding). The pooled representation is then passed through a readout network that produces the logit $z \in \mathbb{R}$, which maps to the predicted probability $P(\lambda = 1 \mid \sigma) = \sigma(z) = 1/(1 + e^{-z})$. The predicted observable is $\hat{\lambda} = \mathbb{I}[\sigma(z) > 0.5]$. We employ two readout variants: a ResBlock readout consisting of L_{res} residual blocks with hidden dimension d_{read} , and a simpler MLP readout with a single hidden layer.

For depolarizing noise with perfect stabilizer measurements (Section 4.1), we use a dual-head decoder that predicts both the Z-type logical observable λ_Z and the X-type logical observable λ_X from a shared backbone representation, following the setup of Lange et al. [15].

3.2 Training Protocol

We employ three training protocols depending on the noise model and data source.

For uniform circuit-level and depolarizing noise benchmarks, we train from scratch with fresh synthetic data generated each epoch. The physical error rate is sampled uniformly from a training set (e.g., $p \in \{0.001, 0.002, \dots, 0.005\}$) following Lange et al. [15]. We use AdamW with cosine learning rate annealing over 500–1000 epochs, with $4\text{--}6 \times 10^6$ freshly generated samples per epoch.

For the SI1000 benchmark, we train with a three-stage curriculum over measurement rounds: the maximum round count increases from $r \leq 9$ (Stage 1) to $r \leq 25$ (Stage 2) to $r \leq 120$ (Stage 3) at transitions of 500K and 1M iterations. The physical error rate is sampled uniformly from $p \in \{0.001, 0.002, 0.003, 0.005, 0.007, 0.01\}$ at each training step. We use the Lion optimizer [21] with constant learning rate 5×10^{-6} and EMA decay 0.9999. The best checkpoint is selected by evaluating all saved checkpoints (every 50K steps) on 10^5 fresh samples at the target error rate; the best checkpoints were typically found at 2.3–2.9M iterations depending on distance.

For experimental data from Sycamore, we follow a two-stage protocol adapted from AlphaQubit [10, 11]. The first stage pretrains on synthetic data sampled from a Detector Error Model (DEM) calibrated to the target hardware via XEB calibration data, using a round curriculum analogous to SI1000 (Stage 1: $r \leq 9$, Stage 2: $r \leq 17$, Stage 3: $r \leq 25$, with transitions at 150K and 300K iterations). The second stage finetunes on real experimental data with a reduced learning rate (2×10^{-6}) and zero weight decay.

Following AlphaQubit 2 [11], we apply BERT-style input masking during SI1000 training and Sycamore pretraining: with probability 0.8, we zero out 50% of randomly selected defect features. This regularization technique encourages the model to learn robust representations from partial information.

For SI1000 and Sycamore, we scale the base learning rate according to sequence length, following AlphaQubit 2 [11]:

$$\text{lr}_{\text{eff}} = \text{lr}_{\text{base}} \times 0.8^{\log_2(N_s/8)} \times 2^{\log_2(R/24)}, \quad (12)$$

where N_s is the number of stabilizers and R is the number of rounds, capped at a maximum scaling factor of $5\times$.

4 Experiments

We evaluate the Sparse Mamba Decoder across four benchmarks of increasing complexity, from idealized noise models to real experimental data. Training was conducted on a mix of consumer and datacenter GPUs depending on model size: the depolarizing ($\sim 7.7\text{M}$ parameters), uniform circuit-level ($\sim 7.6\text{M}$), and Sycamore ($\sim 7.6\text{M}$) models were trained on a single NVIDIA RTX 4090 (24GB), while the larger SI1000 model ($\sim 16\text{M}$ parameters for $d \geq 5$, with $R = 120$ rounds) required a single NVIDIA H200 NVL (141GB). Speed benchmarks under SI1000 noise

Table 1: Architecture hyperparameters across the four experimental settings.

Parameter	Symbol	Sycamore	SI1000	Circuit-level	Depolarizing
Model dimension	d_{model}	320	320/384*	320	320
Mamba layers	L	4	4/6*	4	4
Mamba state dim	d_{state}	16	16	16	16
Mamba conv width	d_{conv}	4	4	4	4
Mamba expand	–	2	2	2	2
Gate widening	w_{gate}	5	5	5	5
Input features	–	13	13	13	13
Readout type	–	ResBlock	ResBlock	MLP	Dual MLP
Output heads	–	1	1	1	2 (λ_Z, λ_X)
Dropout	–	0.1	0.1	0.1	0.1
Parameters	–	$\sim 7.6\text{M}$	$7.5/16\text{M}^*$	$\sim 7.6\text{M}$	$\sim 7.7\text{M}$

*SI1000: $d_{\text{model}} = 320, L = 4, \sim 7.5\text{M}$ params for $d = 3$; $d_{\text{model}} = 384, L = 6, \sim 16\text{M}$ params for $d \geq 5$.

(Section 4.5) were measured on the H200; speed benchmarks under uniform circuit-level noise were measured on the RTX 4090.

Architecture and training hyperparameters are summarized in Tables 1 and 2, and Table 3 situates SMD against existing ML-based decoders in terms of input representation, complexity, and hardware requirements. All circuit-level noise models and Monte Carlo sampling use the Stim simulator [22]; baseline matching decoders use PyMatching [7], Belief Matching [19], and Tesseract [9]. For uniform circuit-level (Section 4.2) and depolarizing (Section 4.1) benchmarks, we report the logical error rate (LER) as the per-shot failure fraction $\text{LER} = E_{\text{fail}}/N$, following Lange et al. [15]. For SI1000 (Section 4.3) we report per-cycle LER following AlphaQubit 2 [11], and for Sycamore (Section 4.4) per-round LER via log-fidelity regression following Lee et al. [13]. For SI1000 speed comparisons (Section 4.5, Table 9 and Figure 6), we report the frame error rate (FER), identical to per-shot LER for a single memory experiment, following AlphaQubit 2 [11]. The uniform circuit-level speed comparison (Figure 7) uses per-shot LER as in Section 4.2. Unless otherwise stated, statistical uncertainties on Monte Carlo estimates are reported as 95% binomial confidence intervals; for the Sycamore log-fidelity regression, uncertainty is estimated from the regression standard error.

4.1 Depolarizing Noise with Perfect Stabilizers

We first evaluate on the simplest noise model, following Lange et al. [15] (Figure 8 therein). Data qubits experience depolarizing noise $\mathcal{E}(\rho) = (1-p)\rho + \frac{p}{3}(X\rho X + Y\rho Y + Z\rho Z)$ with perfect (noiseless) stabilizer measurements, producing a purely spatial decoding problem with a single round. The decoder predicts both logical observables λ_Z and λ_X using the dual-head variant. For this single-round setting, the 13th feature (reconstructed measurement) equals 1.0 at all defect positions, since a single detection event that fired trivially gives $m_{i,1} = d_{i,1} = 1$.

Figure 3 shows the logical error rates across all distances and error rates. SMD outperforms MWPM at every distance and error rate tested, with improvement increasing monotonically with code distance: from 6–15% at $d = 3$ to 17–91% at $d = 11$.

A striking finding is that MWPM, the Tesseract near-MLD decoder [9], and Belief Matching [19] all achieve nearly identical logical error rates across all distances and error rates (Table 4). This suggests that MWPM is already near-optimal among factorized independent-basis decoders for the rotated surface code with depolarizing noise and perfect stabilizers, consistent with the observation by Lange et al. that their GNN decoder converges to approximate MLD accuracy at $d \leq 5$.

The classical decoders decode λ_Z and λ_X independently: MWPM performs separate matching on the Z-stabilizer and X-stabilizer syndrome graphs. Our decoder, in contrast, receives both syn-

Table 2: Training hyperparameters across the four experimental settings. Sycamore uses DEM-based pretraining followed by finetuning on experimental data; the iterations row reports the DEM-pretraining stage. SI1000 training is stopped when validation LER plateaus, typically at 2.3–2.9M iterations depending on distance. The remaining settings train from scratch on synthetic data.

Parameter	Sycamore	SI1000	Circuit-level	Depolarizing
<i>Training</i>				
Optimizer	Lion	Lion	AdamW	AdamW
Learning rate	5×10^{-6}	5×10^{-6}	5×10^{-5} – 10^{-4}	1×10^{-4}
LR schedule	constant	constant	cosine	cosine
Iterations	1–4M [‡]	2.3–2.9M	—	—
Training epochs	—	—	600–1000	500
Samples/epoch	—	—	1–6M	1–3M
Batch size	128–256	256–512	128–512	512
Train error rates	—	[.001–.01]	[.001–.005]	[.01,.05,.10,.15]
Mixed rates	—	yes	yes	yes
EMA decay	0.9999	0.9999	off	off
Weight decay	10^{-5}	10^{-5}	10^{-2}	10^{-2}
Gradient clipping	1.0	1.0	1.0	1.0
Curriculum stages	3 (150K/stage)	3 (500K/stage)	—	—
Training noise model	DEM	SI1000	uniform	depolarizing
<i>Finetuning (Sycamore only)</i>				
Finetune LR	2×10^{-6}	—	—	—
Finetune epochs	10	—	—	—
FT split ($d=3$)	50/50	—	—	—
FT split ($d=5$)	80/20	—	—	—
<i>Inference</i>				
Ensemble size	5/16*	3 [†]	—	—

*Sycamore: 5 models for $d = 3$, 16 for $d = 5$.

[†]SI1000: 3-checkpoint ensemble for $d = 7$ only (steps 2.65M, 2.85M, 2.90M).

[‡]Sycamore: 1M iterations for $d = 3$, 4M for $d = 5$.

drome types as input and predicts (λ_Z, λ_X) jointly. Under depolarizing noise, Y errors (occurring with probability $p/3$) simultaneously trigger both Z -type and X -type stabilizers, creating correlated defect patterns across the two syndrome types. The Mamba backbone naturally captures these Y -error correlations through its joint sequence processing, which independent matching decoders structurally cannot exploit. This explains how SMD surpasses the near-optimal accuracy of independent decoding by 40–91% at larger distances. We emphasize that joint decoding is a structural advantage of neural decoders: matching-based decoders (MWPM, Tesseract, Belief Matching) are fundamentally factorized into independent X - and Z -graph matchings, whereas a single neural backbone can model the cross-basis correlations introduced by Y errors. The 40–91% improvement therefore reflects both the sparse representation and the architectural capacity to exploit correlations inaccessible to factorized matching decoders.

4.2 Circuit-Level Noise (Uniform)

We next evaluate on circuit-level noise following Lange et al. [15] (Figure 4 therein), where all operations (two-qubit gates, single-qubit gates, measurements, resets) experience the same depolarizing rate p . The number of stabilizer measurement rounds equals the code distance ($R = d$), and the decoder predicts a single logical observable λ_Z from a Z -basis memory experiment.

We compare against MWPM (PyMatching [8]), the standard matching-based baseline. SMD uses a single-head variant predicting λ_Z only, with $d_{\text{model}} = 320$, $L = 4$ layers, and expand

Table 3: Comparison of decoder architectures by input representation, complexity, and hardware. Here n denotes the syndrome size or number of detection events, B is the Tesseract beam-search width, and M is the Libra ensemble size. Our sparse approach yields $\mathcal{O}(k)$ with $k \ll d^2R$.

Decoder	Params	Input	Complexity	Hardware
<i>Classical decoders (no learned parameters)</i>				
MWPM (PyMatching)	—	Detection events	$\mathcal{O}(n \log n)$	CPU
Tesseract	—	DEM graph	$\mathcal{O}(n \cdot B)$	CPU
Libra [20]	—	Detection events	$\mathcal{O}(n \log n \cdot M)$	CPU
<i>Neural decoders</i>				
AlphaQubit 1	5.4M	Dense $d^2 \times R$	$\mathcal{O}(d^4 R)$	TPU v5e
AlphaQubit 2 (full)	~ 32 M	Dense $d^2 \times R$	$\mathcal{O}(d^2 R)$	Trillium TPU
AlphaQubit 2 (RT)	~ 10 M	Dense $d^2 \times R$	$\mathcal{O}(d^2 R)$	Trillium TPU
Dense Mamba	~ 5 – 10 M	Dense $d^2 \times R$	$\mathcal{O}(d^2 R)$	RTX 4090
Proposed SMD	7.5–16M	Sparse k defects	$\mathcal{O}(k)$	RTX 4090 / H200

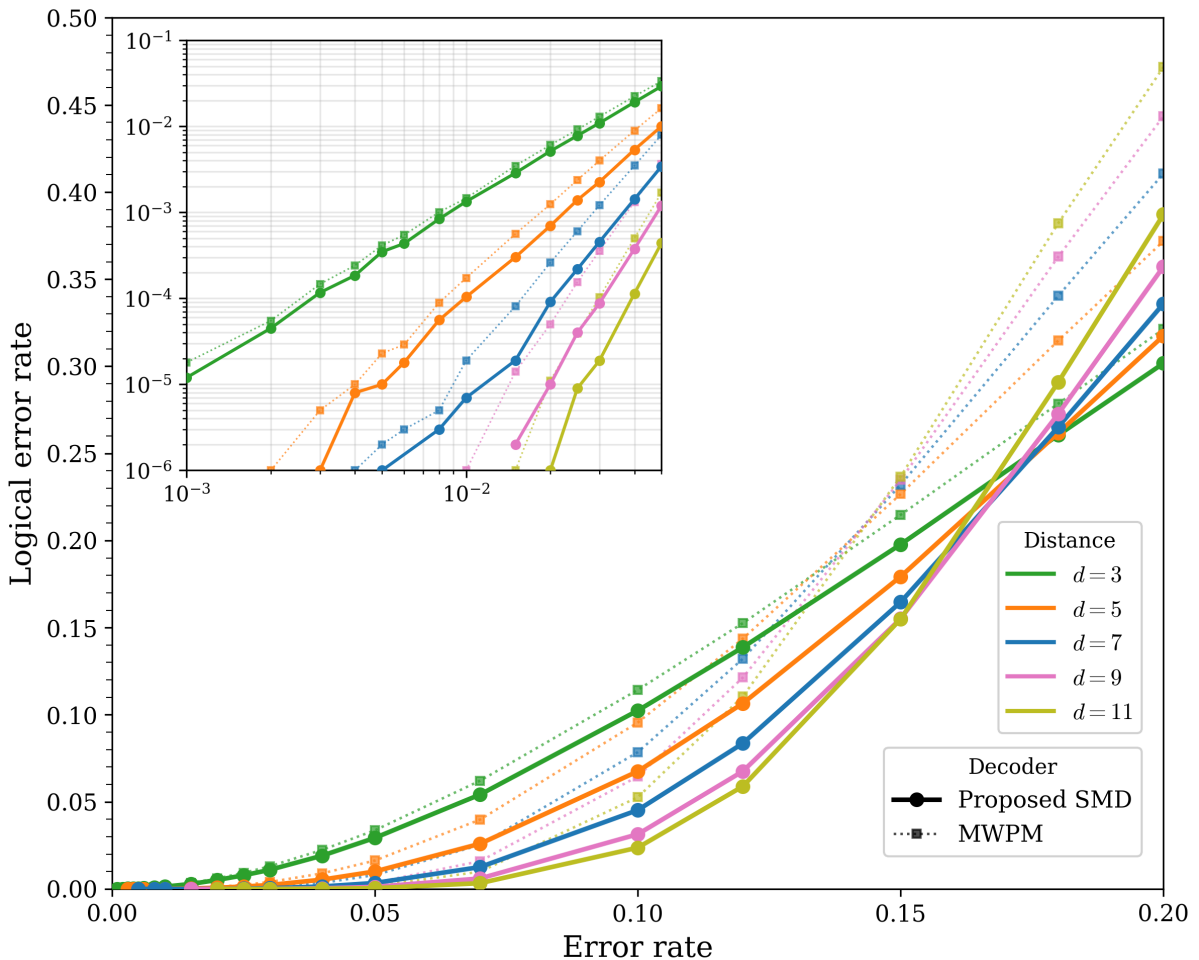


Figure 3: Logical error rate under depolarizing noise with perfect stabilizer measurements. The Sparse Mamba Decoder (solid lines) with dual prediction heads for λ_Z and λ_X is compared against MWPM (dotted) at distances $d \in \{3, 5, 7, 9, 11\}$. Each data point is evaluated over 10^6 – 3×10^6 fresh samples. *Inset*: Log-log view of the low- p region, showing the widening gap between SMD and MWPM with increasing distance.

Table 4: Decoder comparison under depolarizing noise with perfect stabilizers (combined failure: wrong λ_Z or wrong λ_X). All three classical decoders achieve nearly identical error rates, confirming MWPM is near-optimal for independent-basis decoding. SMD outperforms all through joint (λ_Z, λ_X) prediction. Bold indicates the best result per cell. A dash indicates fewer than one failure in 3×10^6 samples.

		$d=3$	$d=5$	$d=7$	$d=9$	$d=11$
$p=.01$	MWPM	1.5e-3	1.7e-4	1.9e-5	1e-6	—
	Tesseract	1.5e-3	1.7e-4	1.9e-5	1e-6	—
	Belief Match.	1.5e-3	1.8e-4	2.0e-5	1e-6	—
	Mamba	1.3e-3	1.0e-4	7e-6	—	—
$p=.03$	MWPM	1.3e-2	4.0e-3	1.2e-3	3.6e-4	1.0e-4
	Tesseract	1.3e-2	4.1e-3	1.2e-3	3.7e-4	1.0e-4
	Belief Match.	1.3e-2	4.1e-3	1.2e-3	3.6e-4	1.1e-4
	Mamba	1.1e-2	2.3e-3	4.6e-4	8.8e-5	1.9e-5
$p=.05$	MWPM	3.4e-2	1.6e-2	8.0e-3	3.7e-3	1.7e-3
	Tesseract	3.5e-2	1.7e-2	7.9e-3	3.8e-3	1.7e-3
	Belief Match.	3.5e-2	1.7e-2	8.1e-3	3.7e-3	1.9e-3
	Mamba	2.9e-2	1.0e-2	3.4e-3	1.2e-3	4.4e-4
$p=.10$	MWPM	1.1e-1	9.6e-2	7.9e-2	6.5e-2	5.3e-2
	Tesseract	1.2e-1	9.8e-2	8.0e-2	6.6e-2	5.3e-2
	Belief Match.	1.2e-1	1.0e-1	8.1e-2	6.6e-2	5.4e-2
	Mamba	1.0e-1	6.8e-2	4.5e-2	3.1e-2	2.4e-2

factor 2. Training uses AdamW with cosine learning rate annealing over 600–1000 epochs, with $1\text{--}6 \times 10^6$ freshly generated samples per epoch and error rates sampled uniformly from $p \in \{0.001, 0.002, 0.003, 0.004, 0.005\}$. Each data point is evaluated over $4\text{--}6 \times 10^6$ fresh samples.

SMD outperforms MWPM at every distance and error rate tested (Figure 4), with LER ratios (SMD/MWPM) ranging from 0.70 at $d = 3$ to 0.47 at $d = 7$ at the lowest error rate ($p = 0.001$). The improvement is consistent across all rates: at $p = 0.003$, SMD reduces the logical error rate by 18% at $d = 3$, 39% at $d = 5$, 44% at $d = 7$, and 25% at $d = 9$. At $d = 9$, $p = 0.005$, SMD essentially matches MWPM (ratio 0.98). A speed–accuracy comparison with Belief Matching [19], which achieves lower rates at $d \geq 7$ but at 18–230 \times higher latency for $d \geq 5$, is presented in Section 4.5.

The GNN decoder of Lange et al. [15] trained each model for 1000 epochs with 10^7 freshly generated samples per epoch, totaling 10^{10} training samples per distance. In contrast, SMD uses 6×10^8 samples at $d = 3$ ($600 \text{ epochs} \times 10^6$), 1.2×10^9 at $d = 5$ ($600 \times 2 \times 10^6$), 1.8×10^9 at $d = 7$ ($600 \times 3 \times 10^6$), and 6×10^9 at $d = 9$ ($1000 \times 6 \times 10^6$)—a 1.7–17 \times reduction in training data. Despite this, SMD outperforms MWPM at all distances and error rates, whereas the GNN decoder of Lange et al. reports performance approximately matching MWPM (their Figure 4 does not provide exact numerical values, precluding a direct quantitative comparison). At $d = 9$, where our training budget is 60% of the reference, SMD outperforms MWPM for $p \leq 0.004$ (ratios 0.63–0.86) and essentially matches MWPM at $p = 0.005$ (ratio 0.98); the remaining gap is consistent with the reduced training budget rather than a fundamental architectural limitation.

4.3 Circuit-Level Noise (SI1000)

To enable direct comparison with AlphaQubit 2 [11] and the Tesseract near-MLD baseline [9] (compared on speed–accuracy in Section 4.5), we evaluate on the SI1000 noise model (a superconducting-inspired noise model with asymmetric error rates, Table 5), which is the standard benchmark used by recent high-accuracy decoders. We test at $p = 1.5 \times 10^{-3}$, representative of near-term

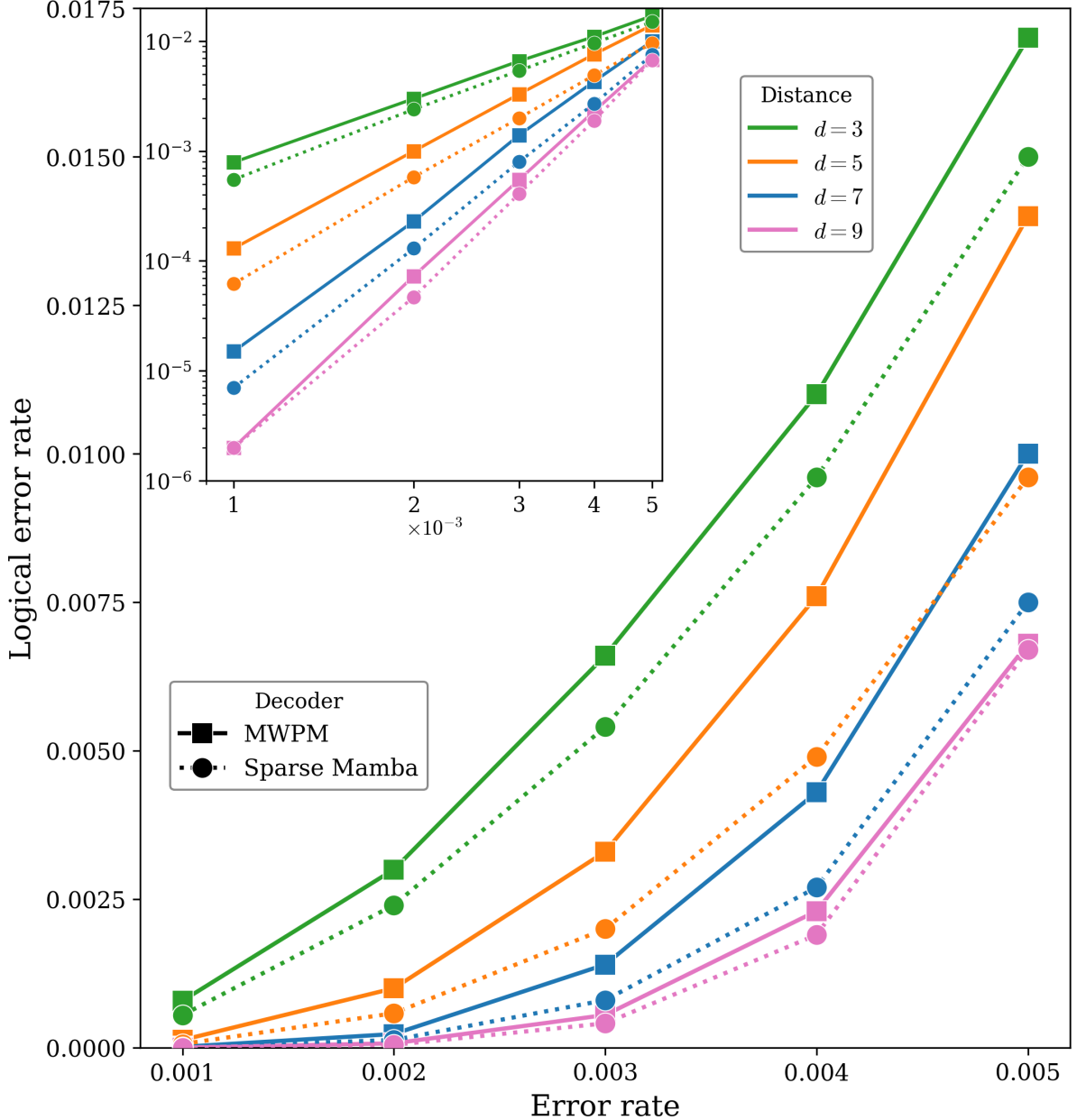


Figure 4: Logical error rate under uniform circuit-level noise with $R = d$ stabilizer measurement rounds. SMD (dotted circles) vs MWPM (solid squares) at distances $d \in \{3, 5, 7, 9\}$ and error rates $p \in [0.001, 0.005]$. SMD outperforms MWPM at all distances and rates.

hardware operating conditions and well below the SI1000 surface-code threshold ($p_{\text{th}} \approx 5 \times 10^{-3}$ for our $R = 120$ setup), with code distances $d \in \{3, 5, 7\}$, $R = 120$ stabilizer measurement rounds, and 5×10^5 Monte Carlo shots per configuration.

For the SI1000 benchmark, we train with a three-stage curriculum over measurement rounds: the maximum round count increases from $r \leq 9$ (Stage 1) to $r \leq 25$ (Stage 2) to $r \leq 120$ (Stage 3) at transitions of 500K and 1M iterations. We use the Lion optimizer [21] with constant learning rate 5×10^{-6} and EMA decay 0.9999. The best checkpoint is selected by evaluating all saved checkpoints (every 50K steps) on 10^5 fresh samples at the target error rate; training is stopped when validation LER plateaus, with the best checkpoints typically found at 2.3–2.9M iterations depending on distance.

For $d = 7$, where single-model performance is close to MWPM, we employ multi-checkpoint

Table 5: SI1000 noise model error rates relative to the base two-qubit gate rate p (following [11]).

Operation	Rate	Description
Two-qubit gate (CZ)	p	Two-qubit depolarizing
Single-qubit gate	$p/10$	Single-qubit depolarizing
Measurement readout	$5p$	Bit-flip before readout
Reset	$2p$	Bit-flip after reset
Idle (per round)	$4.2p$	Combined idle depolarizing

Table 6: Logical error rate per cycle under SI1000 noise at $p = 1.5 \times 10^{-3}$, $R = 120$. Ratio is LER relative to MWPM. Relative 95% binomial CIs are approximately $\pm 7\%$, $\pm 16\%$, and $\pm 23\%$ at $d = 3, 5, 7$ respectively. **Bold** indicates best neural decoder per distance; classical matching baselines shown for reference.

Decoder	$d = 3$	$d = 5$	$d = 7$
MWPM (PyMatching)	2.21×10^{-3}	6.20×10^{-4}	1.71×10^{-4}
Corr. Matching [†]	1.57×10^{-3} (0.71 \times)	3.42×10^{-4} (0.55 \times)	7.45×10^{-5} (0.44 \times)
Libra-7 (MWPM ensemble)	2.21×10^{-3} (1.00 \times)	6.20×10^{-4} (1.00 \times)	1.71×10^{-4} (1.00 \times)
Proposed SMD (single)	1.43×10^{-3} (0.65 \times)	3.14×10^{-4} (0.51 \times)	1.70×10^{-4} (0.99 \times)
Proposed SMD (ensemble)	1.43×10^{-3} (0.65 \times)	3.16×10^{-4} (0.51 \times)	1.44×10^{-4} (0.84 \times)

[†]Evaluated with $N = 10^4$ due to cost (327 ms/shot).

ensembling: we average the output logits of three models taken from different training steps (2.65M, 2.85M, 2.90M), which provide genuine diversity since models at different points in training have learned qualitatively different feature representations. This approach is analogous to the multi-seed ensembling used for Sycamore (Section 4.4), but exploits checkpoint diversity rather than seed diversity.

Table 6 presents the SI1000 results. At $d = 3$ and $d = 5$, the single-model SMD outperforms MWPM, achieving LER ratios of 0.65 and 0.51 respectively. At $d = 7$, the single model approximately matches MWPM (ratio 0.99); the three-checkpoint ensemble reduces the LER to 1.44×10^{-4} , a 16% improvement over MWPM though within statistical uncertainty ($\pm 24\%$ relative 95% CI at this LER and sample size). Correlated Matching (Belief Matching) provides a stronger baseline at $d = 7$, achieving 7.45×10^{-5} (ratio 0.44), but at $d \leq 5$ SMD outperforms it: ratio 0.65 vs. 0.71 at $d = 3$ and 0.51 vs. 0.55 at $d = 5$. Ensembling provides meaningful gains only when the single model is uncertain or near saturation; we additionally evaluated multi-checkpoint ensembling at $d = 3$ and $d = 5$ and observed no significant further improvement, consistent with the single-model SMD already being substantially better than MWPM at these distances.

We also compare against a Libra-style ensemble decoder [20], which creates diversity by perturbing the edge weights of the detector error model and combining multiple MWPM solutions via majority vote. Despite using 7 ensemble members, the Libra-style decoder shows negligible improvement over standard MWPM at all distances ($< 0.5\%$), confirming that the matching-based approach has saturated its accuracy on this noise model. In contrast, our neural ensemble captures error correlations inaccessible to matching-based methods, yielding a 16% LER reduction at $d = 7$.

Round dependence

A distinctive feature of the sparse decoder is that its performance depends not only on code distance but also on the number of measurement rounds, which directly controls the defect sequence length k . Table 7 shows the LER ratio (SMD/MWPM) as a function of rounds for

Table 7: LER ratio (SMD / MWPM) as a function of measurement rounds under SI1000 noise at $p = 1.5 \times 10^{-3}$, $N = 10^5$ shots. Values below 1.0 indicate SMD outperforms MWPM. Model trained with $r \leq 120$; $r = 140$ tests out-of-distribution generalization.

	$r = 10$	$r = 25$	$r = 50$	$r = 80$	$r = 120$	$r = 140^*$
$d = 5$	7.93	1.88	0.72	0.52	0.52	0.54
$d = 7$	0.81	0.84	0.77	0.84	0.99	1.40

*Beyond training range ($r_{\max} = 120$).

Table 8: LER ratio (SMD / MWPM) as a function of physical error rate under SI1000 noise at $R = 120$, $N = 10^5$ shots ($N = 5 \times 10^5$ for $d = 7$). Values below 1.0 indicate SMD outperforms MWPM.

	$p = 0.001$	$p = 0.0015$	$p = 0.002$	$p = 0.003$
$d = 3$	0.65	0.66	0.68	0.71
$d = 5$	0.51	0.51	0.53	0.61
$d = 7$	0.90	0.99	1.45	2.08

$d = 5$ and $d = 7$.

At $d = 5$, SMD *loses* to MWPM at short rounds ($r \leq 25$, ratio > 1) but *wins* decisively at long rounds ($r \geq 50$, ratio ≈ 0.5). This is because at short rounds with low p , the expected number of defects is very small ($k \approx 7$ at $r = 10$), providing insufficient signal for the learned model—MWPM’s structural knowledge of the error model compensates for its inability to learn correlations. At $d = 7$, the sparse decoder beats MWPM at $r \leq 80$ (ratio 0.77–0.84) and matches MWPM at $r = 120$ (ratio 0.99). Only beyond the training range at $r = 140$ does performance degrade significantly (ratio 1.40), as the defect count exceeds the model’s training distribution. Multi-checkpoint ensembling recovers strong performance even at $r = 120$, reducing the ratio to 0.84. Notably, at $d = 5$ the model generalizes beyond its training range: performance at $r = 140$ (not seen during training, which used $r \leq 120$) remains strong (ratio 0.54), demonstrating that the learned representations extrapolate to longer sequences.

Table 8 shows the LER ratio as a function of physical error rate. At $d = 3$ and $d = 5$, SMD outperforms MWPM across all sub-threshold rates, with low ratios of 0.65–0.71 at $d = 3$ and 0.51–0.61 at $d = 5$. At $d = 7$, SMD wins only at the lowest rate ($p = 0.001$, ratio 0.90) where the syndrome is sparsest ($k \approx 185$ mean defects). At higher rates, the growing defect count exceeds the model’s effective capacity, consistent with the round-dependence analysis above.

4.4 Sycamore Experimental Data

We evaluate on the publicly available Sycamore memory experiment dataset [6, 10], which comprises 50,000 shots per round setting across four distance-3 patches (north/south/east/west) and one distance-5 patch, for both X- and Z-basis memory experiments with rounds $R \in \{1, 3, 5, \dots, 25\}$. This experiment provides a direct comparison with the dense Mamba decoder of Lee et al. [13], which reports LERs of 2.98×10^{-2} (distance 3) and 3.03×10^{-2} (distance 5), averaged across X and Z bases. We follow an identical evaluation protocol: DEM-based pre-training from XEB calibration data, finetuning on experimental data, and LER computation via log-fidelity regression across rounds $\{3, 5, \dots, 25\}$, excluding round 1 due to time-boundary effects.

We pretrain using a curriculum learning strategy over rounds: Stage 1 ($r \in \{3, 5, 7, 9\}$), Stage 2 ($r \leq 17$), and Stage 3 ($r \leq 25$), with transitions at 150K and 300K iterations following Lee et al. [13]. For distance 3, we pretrain for 1M iterations with batch size 256; for distance 5, we extend pretraining to 4M iterations with batch size 128, as the single distance-5 patch provides

only 600K experimental samples (compared to 2.4M for the four distance-3 patches), requiring stronger pretrained representations to compensate for limited finetuning data. During finetuning, we use the Lion optimizer with learning rate 2×10^{-6} and zero weight decay. For distance 3, we use a 50/50 train/evaluation split (1.2M training samples); for distance 5, we use an 80/20 split (480K training samples) to maximize the training set given the limited data from a single patch.

Following standard practice in neural QEC decoding [10, 11], we improve prediction accuracy through model ensembling. We finetune multiple models from the same pretrained checkpoint using different random seeds (which produce different train/evaluation splits), then average their output logits at inference time. Additionally, we finetune models from pretrained checkpoints at different training stages (3M, 3.5M, and 4M steps for distance 5), which provides genuine model diversity beyond what seed variation alone can achieve—models at different points in pretraining have learned qualitatively different feature representations. Our final ensemble combines 16 models per basis (10 from the 4M checkpoint with different seeds, plus 3 each from the 3M and 3.5M checkpoints). For distance 3, we ensemble 5 models per basis.

The proposed SMD achieves a mean LER of 2.940×10^{-2} at distance 3 and 3.001×10^{-2} at distance 5 (ensemble, averaged across bases), matching or surpassing the dense Mamba decoder of Lee et al. (2.98×10^{-2} and 3.03×10^{-2} , respectively) despite using a sparse input representation without dilated 2D convolutions. At distance 3, our decoder outperforms all baselines including the tensor network decoder (3.053×10^{-2}). At distance 5, our ensemble result surpasses belief matching (3.109×10^{-2}) and the dense Mamba decoder, and comes within 0.6% of the tensor network decoder (2.983×10^{-2}). Single-model results without ensembling also demonstrate strong performance: 3.015×10^{-2} at distance 3 and 3.130×10^{-2} at distance 5. The single model surpasses correlated matching and belief matching at distance 3 and correlated matching at distance 5; ensembling is required to surpass belief matching and dense Mamba at distance 5. Ensembling provides a $\sim 2.5\%$ relative LER improvement at distance 3 and $\sim 4\%$ at distance 5. SMD ensemble achieves the lowest LER among all compared decoders at distance 3, and the second-lowest at distance 5 (behind only the tensor network). Figure 5 summarizes the comparison.

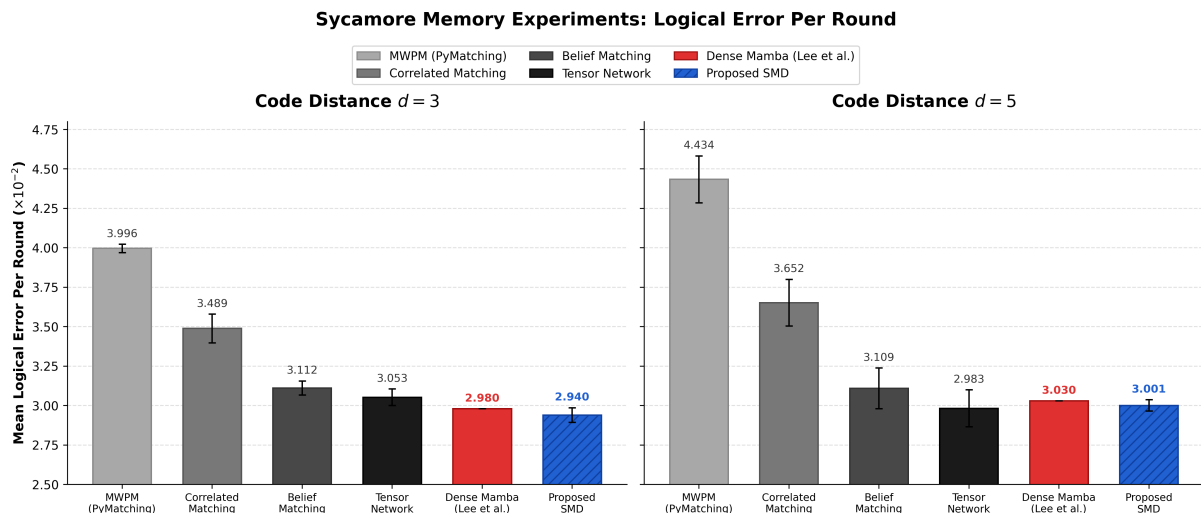


Figure 5: Mean logical error per round on the Google Sycamore experimental dataset at code distances 3 and 5. Results are averaged across X and Z bases. Error bars indicate the spread between bases. The proposed Sparse Mamba Decoder (blue, hatched) matches or outperforms the dense Mamba decoder of Lee et al. [13] (red) at both distances, despite processing only active defects with $\mathcal{O}(k)$ complexity compared to $\mathcal{O}(d^2R)$ for dense approaches.

4.5 Computational Efficiency

A key advantage of the sparse representation is reduced computational cost at physically relevant error rates. Table 9 reports end-to-end decoding time and FER for MWPM, Belief Matching [19], Tesseract, and SMD at $d \in \{3, 5, 7\}$ under SI1000 noise at $p = 10^{-3}$, $R = 120$, on a single NVIDIA H200 NVL GPU. SMD achieves two-to-three orders of magnitude speedup over near-MLD decoders while approaching their accuracy (Figure 6).

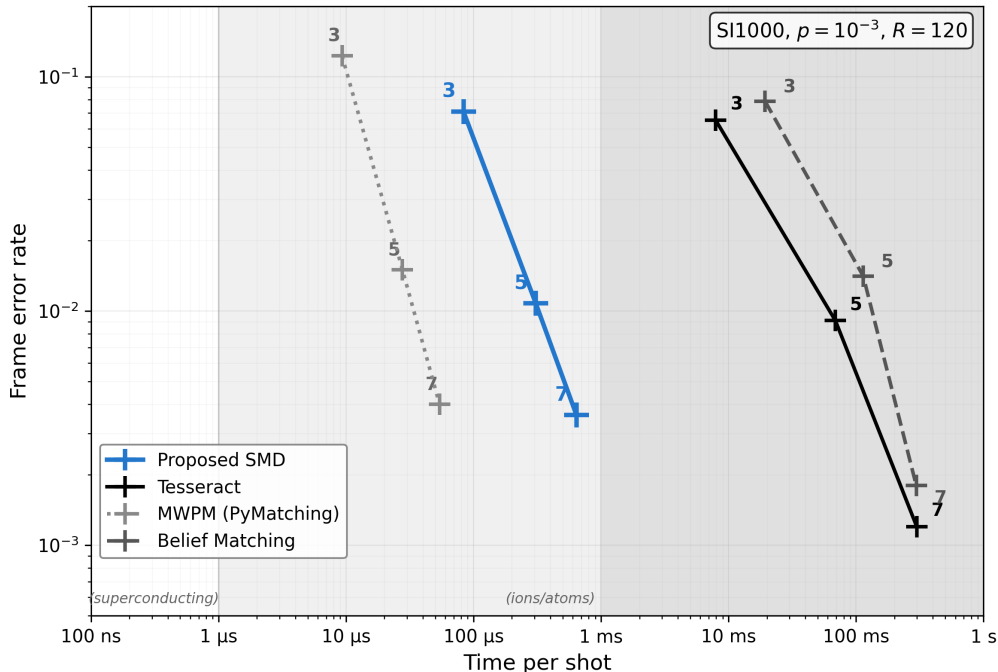


Figure 6: Speed–accuracy Pareto front for MWPM, Belief Matching, Tesseract, and SMD at $d \in \{3, 5, 7\}$ under SI1000 noise at $p = 10^{-3}$, measured on NVIDIA H200 NVL. Lower-left is better. Vertical lines at $1 \mu\text{s}$ and 1ms separate the superconducting, trapped-ion/atom, and offline regimes. SMD occupies the ions/atoms regime ($100 \mu\text{s}$ – 1ms), achieving lower FER than MWPM while running 95–467 \times faster than Tesseract and 232–463 \times faster than Belief Matching. Distance labels indicate $d \in \{3, 5, 7\}$.

SMD’s defect-centric representation yields favorable scaling with code distance. The SMD-to-Tesseract speedup grows from 95 \times at $d = 3$ to 467 \times at $d = 7$, while SMD-to-BM grows from 232 \times to 463 \times . Notably, SMD captures a substantial fraction of Tesseract’s accuracy advantage at orders of magnitude lower latency: at $d = 3$, SMD closes roughly 90% of the FER gap between MWPM and Tesseract (12.3% \rightarrow 7.1% vs. 6.5%); at $d = 5$, $\sim 71\%$ of the gap is closed at 224 \times lower latency than Tesseract. This follows directly from algorithmic complexity: Tesseract’s beam search cost grows with the detector graph size ($\Theta(d^2R)$) and error density, whereas SMD’s forward pass scales with the number of active defects k , which grows as $\mathcal{O}(p \cdot d^2R)$. At fixed p , the ratio $k/(d^2R)$ remains approximately constant across distances (Table 10), so SMD’s per-shot cost grows much more slowly with d than competing decoders.

Under uniform circuit-level noise at $p = 0.002$ (Figure 4), SMD latency increases only 2.4 \times from $d = 3$ to $d = 9$ ($24 \mu\text{s}$ to $57 \mu\text{s}$ on an NVIDIA RTX 4090), compared to 773 \times for Belief Matching ($17 \mu\text{s}$ to 13.1ms on a single CPU core). At $d = 9$, SMD decodes 230 \times faster than Belief Matching, while outperforming both MWPM and Belief Matching in accuracy at $d \leq 7$ (Figure 7).

At single-shot latency (batch size 1), SMD requires 4–12 ms per shot, dominated by GPU kernel-launch overhead rather than compute. This is incompatible with the $\sim 1 \mu\text{s}$ per-cycle

Table 9: End-to-end decoding time per shot and frame error rate (FER) under SI1000 noise at $p = 10^{-3}$, $R = 120$. MWPM, BM, and Tesseract on a single CPU core; SMD on H200 NVL GPU including feature-extraction time. See Table 6 for definitive accuracy at $N = 5 \times 10^5$.

Decoder	$d = 3$		$d = 5$		$d = 7$	
	time/shot	FER	time/shot	FER	time/shot	FER
MWPM	9.3 μ s	12.3%	27.7 μ s	1.50%	54.1 μ s	0.40%
Belief Matching	19.4 ms	7.9%	113.8 ms	1.4%	296.5 ms	0.18%
Tesseract	7.94 ms	6.5%	68.9 ms	0.91%	299.3 ms	0.12%
Proposed SMD (b=1024)	83 μs	7.1%	307 μs	1.08%	641 μs	0.36%
Speedup (Tesseract / SMD)	95 \times	—	224 \times	—	467 \times	—
Speedup (BM / SMD)	232 \times	—	370 \times	—	463 \times	—

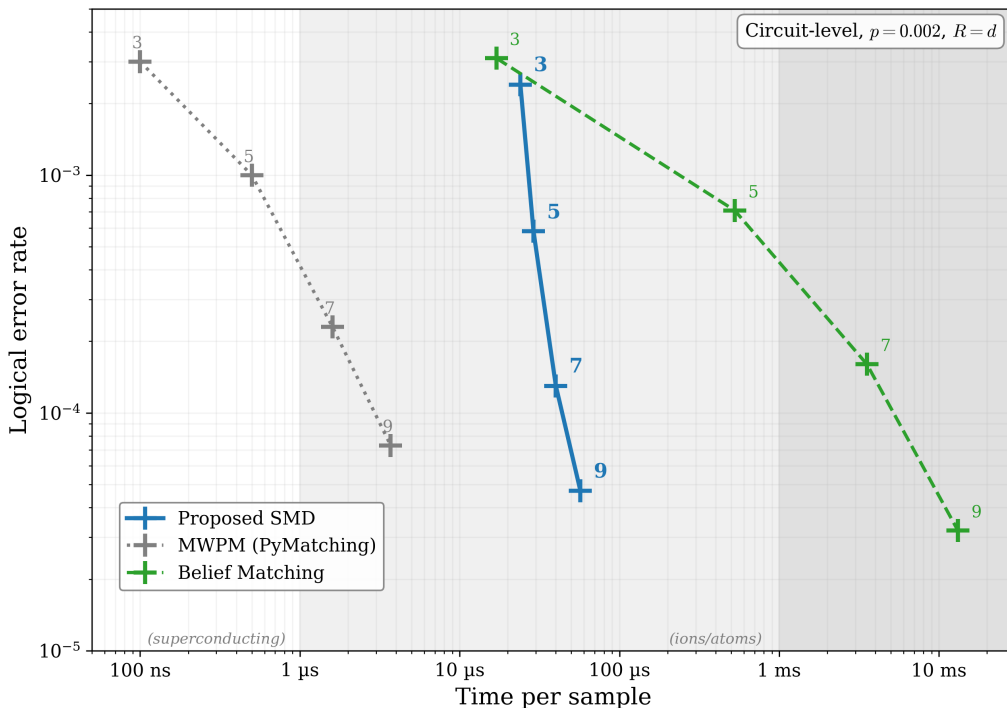


Figure 7: Speed–accuracy Pareto front under uniform circuit-level noise at $p = 0.002$, $R = d$. SMD on RTX 4090; MWPM and BM on a single CPU core. Lower-left is better. SMD (blue) is 18–230 \times faster than Belief Matching (green) for $d \geq 5$ while outperforming MWPM (gray) in accuracy at all distances.

budget of superconducting qubits; a streaming decoder architecture (left to future work) would be required for real-time operation. The throughput numbers in Table 9 are appropriate for offline evaluation, simulation, and syndrome-buffered decoding scenarios.

AlphaQubit 2’s real-time variant (AQ2-RT) [11] achieves sub-microsecond per-cycle throughput, placing it in the superconducting regime. AQ2-RT runs on Google’s Trillium TPU accelerators [12] and employs hardware-specific optimizations including a streaming decoder architecture. The full AQ2 model, which runs in the $\sim 10 \mu$ s regime on the same TPU hardware, is closer in throughput class to SMD’s batched inference. Our goal in this work is not to match AQ2-RT’s specialized-hardware performance, but to demonstrate that high-accuracy neural decoding approaching near-MLD performance can be achieved on a single commodity GPU with a small model (≤ 16 M parameters). The $\mathcal{O}(k)$ scaling of SMD is orthogonal to the streaming architecture of AQ2-RT—both optimizations could in principle be combined in future work to push

Table 10: Effective input size at $p = 10^{-3}$ under SI1000 noise, $R = 120$, $N = 10^5$ shots per cell.

Metric	$d = 3$	$d = 5$	$d = 7$
Stabilizers ($d^2 - 1$)	8	24	48
Dense input size $(d^2 - 1) \times R$	960	2880	5760
Mean defects k (measured)	27.2	89.1	185
99th-percentile k	46	124	235
Sparsity ratio $k/((d^2 - 1)R)$	2.83%	3.09%	3.22%

sparse neural decoding into the sub-microsecond regime.

5 Discussion

5.1 Sparse vs. Dense Mamba

The central comparison of this work is between SMD and the dense Mamba decoder of Lee et al. [13]. Both use the same underlying Mamba state-space model, but differ fundamentally in input representation and spatial processing. The dense Mamba processes the full $(d^2 - 1) \times R$ syndrome array recurrently, with each round’s stabilizer values passed through a stabilizer embedder and then through Syndrome Mixer layers containing Mamba blocks, gated dense layers, and *dilated 2D convolutions* (dilation rates $[1, 1, 2]$ for $d = 5$) that capture multi-scale spatial correlations on the surface code grid, giving complexity $\mathcal{O}(d^2 R)$. SMD, in contrast, processes only k active defects as a 1D sequence sorted by (time, stabilizer index). No convolutions are used—spatial information is encoded entirely in the 13-dimensional feature vector (coordinates, neighbor flags, boundary distances), giving complexity $\mathcal{O}(k)$.

On the Sycamore benchmark, our ensemble decoder achieves LERs of 2.940×10^{-2} (distance 3) and 3.001×10^{-2} (distance 5), matching or surpassing the dense Mamba’s reported 2.98×10^{-2} and 3.03×10^{-2} (Figure 5). This demonstrates that the sparse representation retains sufficient information for accurate decoding, even without the explicit 2D spatial processing provided by dilated convolutions. We attribute this result to two factors. First, the 13-dimensional feature vector encodes rich spatial context—including normalized coordinates, stabilizer type, and binary neighbor flags—that implicitly captures much of the local geometry exploited by convolutions. Second, the Mamba selective scan mechanism learns to correlate defects across the sorted sequence, effectively discovering spatial relationships from the temporal ordering of defects sorted by (time, position).

On the uniform circuit-level noise benchmark, SMD outperforms MWPM by 12–53% across $d = 3$ –7 and the tested error-rate range, while maintaining nearly constant decoding latency (24–57 μ s) across $d = 3$ –9. Under depolarizing noise with perfect stabilizers, the dual-head variant achieves 40–91% lower error rates than MWPM, Tesseract, and Belief Matching at $d = 5$ –11 by exploiting Y -error correlations through joint (λ_Z, λ_X) decoding. The accuracy gap to matching decoders widens with both code distance and decreasing error rate, demonstrating that the sparse representation preserves the structural information needed for high-accuracy decoding.

5.2 Feature Design Rationale

The 13-dimensional defect representation encodes information analogous to what matching-based decoders rely on, while remaining compatible with variable-length sequence processing. The spatial coordinates (x_i, y_i) and stabilizer type τ_i identify *where* and *what kind* of defect occurred—the same information that anchors each node in MWPM’s matching graph. The boundary distances b_Z, b_X encode proximity to the logical operators, which directly determines whether a chain of errors produces a logical failure; matching decoders encode this implicitly through boundary nodes. The four spatial neighbor flags n_1, \dots, n_4 and two temporal neighbor flags

n_5, n_6 provide a local error *fingerprint*: an isolated defect (all flags zero) likely results from a measurement error, while a defect with fired neighbors signals a data qubit error—a distinction that matching decoders make through edge weights in the detector error model. Finally, the reconstructed measurement $m_{i,t}$ via cumulative XOR provides the model with both a *change* signal (the detection event itself) and a *state* signal (the current stabilizer value), following the dual-input approach of AlphaQubit [10]. Together, these features make the geometric structure of the surface code accessible to a purely sequential model, without requiring the learned 2D convolutions that dense decoders rely on to recover spatial context.

5.3 Scalability and Limitations

The sparse approach offers several advantages. Computational cost scales with the number of errors rather than the code size; geometry is encoded directly in the feature vector, eliminating the need for 2D convolutions or spatial embedding; and training and inference run on commodity GPUs without specialized hardware. The result is an $\sim 7.5\text{--}16\text{M}$ parameter decoder that achieves competitive accuracy with $\mathcal{O}(k)$ scaling on a single RTX 4090 or H200 NVL.

Several extensions remain natural directions for future work. Our compute budget restricted experimental evaluation to $d \leq 7$ under SI1000 noise; with additional resources, the same training protocol applies directly to $d = 9, 11$ and beyond. The present architecture also processes the full R -round volume in one pass and is therefore optimized for batched throughput (Table 9) rather than the $\sim 1\ \mu\text{s}$ per-cycle budget required for real-time decoding on superconducting qubits. Reaching that regime would combine SMD’s $\mathcal{O}(k)$ scaling with the streaming, hardware-specific optimizations developed for AQ2-RT [11]—a complementary direction enabled by the small model size and sparse input representation.

This work focuses specifically on the rotated surface code, evaluated on synthetic noise (depolarizing, uniform circuit-level, SI1000) and on Sycamore experimental data. Natural extensions include applying the sparse representation to recent surface-code experiments such as Google’s Willow distance-7 chip [23], where the same three-stage SI1000→DEM→experimental curriculum should transfer directly; adapting the 13-dimensional features for color codes and quantum LDPC codes, where structurally sparser syndromes should make the $\mathcal{O}(k)$ scaling advantage even more pronounced; implementing a streaming variant for real-time decoding; and incorporating soft information (I/Q readout data) for further accuracy gains.

6 Conclusion

We have introduced the Sparse Mamba Decoder, a neural decoder for quantum error correction that processes only active detection events rather than the full dense syndrome array. By representing each defect with 13 engineered features—including spatial coordinates, neighborhood connectivity, boundary distances, and reconstructed measurements via cumulative XOR—and processing the resulting variable-length sequences with a Mamba state-space model, our approach achieves $\mathcal{O}(k)$ computational complexity where k is the number of defects.

Across four benchmarks spanning synthetic noise models and experimental data from Google’s Sycamore quantum processor, SMD demonstrates competitive or superior accuracy compared to existing decoders. Under depolarizing noise with perfect stabilizers, the dual-head variant outperforms MWPM, Tesseract (near-MLD), and Belief Matching by 40–91% at $d = 5\text{--}11$ through joint (λ_Z, λ_X) decoding that exploits Y -error correlations—a structural advantage over matching-based decoders that decode each basis independently. Under uniform circuit-level noise, SMD outperforms MWPM at all distances $d = 3\text{--}9$. On the SI1000 benchmark, it reduces the MWPM logical error rate by up to 49%, and on the Sycamore experimental benchmark, the ensemble matches or slightly surpasses the dense Mamba decoder of Lee et al. despite using a sparse input representation.

A key practical advantage is the decoder’s favorable scaling: under uniform circuit-level noise at $p = 0.002$, latency increases only $2.4\times$ from $d = 3$ to $d = 9$ ($24\mu\text{s}$ to $57\mu\text{s}$ on RTX 4090), compared to $773\times$ for Belief Matching over the same range. At $d = 9$, SMD decodes $230\times$ faster than Belief Matching, while achieving higher accuracy than MWPM. Under SI1000 noise, the speedup over near-MLD decoders grows to $95\text{--}467\times$ (Tesseract) and $232\text{--}463\times$ (Belief Matching). With $\sim 7.5\text{--}16\text{M}$ parameters on commodity NVIDIA GPUs (RTX 4090 for smaller models, H200 for the largest), SMD provides a practical alternative to approaches requiring specialized accelerator hardware.

Our results suggest that the inherent sparsity of quantum error syndromes at physically relevant error rates is a powerful structural prior that should be exploited by decoder architectures. As quantum processors scale to larger code distances, the gap between dense and sparse processing costs will only grow, making defect-centric approaches increasingly attractive. Future work includes adapting the sparse representation for color codes and quantum LDPC codes, implementing a streaming variant for real-time decoding, and combining the $\mathcal{O}(k)$ scaling with hardware-specific optimizations to push sparse neural decoding into the sub-microsecond regime.

References

- [1] Peter W Shor. Scheme for reducing decoherence in quantum computer memory. *Physical Review A*, 52(4):R2493, 1995. doi: 10.1103/PhysRevA.52.R2493. URL <https://doi.org/10.1103/PhysRevA.52.R2493>.
- [2] A Yu Kitaev. Fault-tolerant quantum computation by anyons. *Annals of Physics*, 303(1):2–30, 2003. doi: 10.1016/S0003-4916(02)00018-0. URL [https://doi.org/10.1016/S0003-4916\(02\)00018-0](https://doi.org/10.1016/S0003-4916(02)00018-0).
- [3] Eric Dennis, Alexei Kitaev, Andrew Landahl, and John Preskill. Topological quantum memory. *Journal of Mathematical Physics*, 43(9):4452–4505, 2002. doi: 10.1063/1.1499754. URL <https://doi.org/10.1063/1.1499754>.
- [4] Austin G Fowler, Matteo Mariantoni, John M Martinis, and Andrew N Cleland. Surface codes: Towards practical large-scale quantum computation. *Physical Review A*, 86(3):032324, 2012. doi: 10.1103/PhysRevA.86.032324. URL <https://doi.org/10.1103/PhysRevA.86.032324>.
- [5] Samira Sayedsalehi, Nader Bagherzadeh, Alberto A. Del Barrio, Guillermo Botella, and Ratko Pilipović. Developing and analyzing the defect-based surface codes using optimization algorithms. *Quantum Reports*, 7(2):25, 2025. doi: 10.3390/quantum7020025. URL <https://doi.org/10.3390/quantum7020025>.
- [6] Google Quantum AI. Suppressing quantum errors by scaling a surface code logical qubit. *Nature*, 614:676–681, 2023. doi: 10.1038/s41586-022-05434-1. URL <https://doi.org/10.1038/s41586-022-05434-1>.
- [7] Oscar Higgott and Craig Gidney. Sparse blossom: correcting a million errors per core second with minimum-weight matching. *Quantum*, 9:1600, January 2025. doi: 10.22331/q-2025-01-20-1600. URL <https://doi.org/10.22331/q-2025-01-20-1600>.
- [8] Oscar Higgott. PyMatching: A python package for decoding quantum codes with minimum-weight perfect matching. *ACM Transactions on Quantum Computing*, 3(3):1–16, 2022. doi: 10.1145/3505637. URL <https://doi.org/10.1145/3505637>.
- [9] Laleh Aghababaie Beni, Oscar Higgott, and Noah ShuTTY. Tesseract: A search-based decoder for quantum error correction. *arXiv preprint arXiv:2503.10988*, 2025. doi: 10.48550/arXiv.2503.10988. URL <https://arxiv.org/abs/2503.10988>.

- [10] Johannes Bausch, Andrew W Senior, Francisco JH Heras, Thomas Edlich, Alex Davies, Michael Newman, Cody Jones, Kevin Satzinger, Murphy Yuezhen Niu, Sam Blackwell, et al. Learning high-accuracy error decoding for quantum processors. *Nature*, 635:834–840, 2024. doi: 10.1038/s41586-024-08148-8. URL <https://doi.org/10.1038/s41586-024-08148-8>.
- [11] Andrew W Senior, Thomas Edlich, Francisco JH Heras, Lei M Zhang, Oscar Higgott, James S Spencer, Taylor Applebaum, Sam Blackwell, Justin Ledford, Akvile Zengulyte, Augustin Zidek, Noah Shutty, Andrew Cowie, Yin Li, George Holland, Peter Brooks, Charlie Beattie, Michael Newman, Alex Davies, Cody Jones, Sergio Boixo, Hartmut Neven, Pushmeet Kohli, and Johannes Bausch. A scalable and real-time neural decoder for topological quantum codes. *arXiv preprint arXiv:2512.07737*, 2025. doi: 10.48550/arXiv.2512.07737. URL <https://arxiv.org/abs/2512.07737>.
- [12] Amin Vahdat. Announcing Trillium, the sixth generation of Google Cloud TPU. Google Cloud Blog, May 2024. URL <https://cloud.google.com/blog/products/compute/introducing-trillium-6th-gen-tpus>. Accessed: 2025.
- [13] Changwon Lee, Tak Hur, and Daniel K. Park. Scalable neural decoders for practical real-time quantum error correction. *arXiv preprint arXiv:2510.22724*, 2025. doi: 10.48550/arXiv.2510.22724. URL <https://arxiv.org/abs/2510.22724>.
- [14] Albert Gu and Tri Dao. Mamba: Linear-time sequence modeling with selective state spaces. *arXiv preprint arXiv:2312.00752*, 2024. URL <https://arxiv.org/abs/2312.00752>.
- [15] Moritz Lange, Pontus Havström, Basudha Srivastava, Isak Bengtsson, Valdemar Bergentall, Karl Hammar, Olivia Heuts, Evert van Nieuwenburg, and Mats Granath. Data-driven decoding of quantum error correcting codes using graph neural networks. *Physical Review Research*, 7(2):023181, 2025. doi: 10.1103/PhysRevResearch.7.023181. URL <https://doi.org/10.1103/PhysRevResearch.7.023181>.
- [16] Pavithran Iyer and David Poulin. Hardness of decoding quantum stabilizer codes. *IEEE Transactions on Information Theory*, 61(9):5209–5223, 2015. doi: 10.1109/TIT.2015.2422294. URL <https://doi.org/10.1109/TIT.2015.2422294>.
- [17] Sergey Bravyi, Martin Suchara, and Alexander Vargo. Efficient algorithms for maximum likelihood decoding in the surface code. *Physical Review A*, 90(3):032326, 2014. doi: 10.1103/PhysRevA.90.032326. URL <https://doi.org/10.1103/PhysRevA.90.032326>.
- [18] Nicolas Delfosse and Naomi H Nickerson. Almost-linear time decoding algorithm for topological codes. *Quantum*, 5:595, 2021. doi: 10.22331/q-2021-12-02-595. URL <https://doi.org/10.22331/q-2021-12-02-595>.
- [19] Oscar Higgott, Thomas C Bohdanowicz, Aleksander Kubica, Steven T Flammia, and Earl T Campbell. Improved decoding of circuit noise and fragile boundaries of tailored surface codes. *Physical Review X*, 13(3):031007, 2023. doi: 10.1103/PhysRevX.13.031007. URL <https://doi.org/10.1103/PhysRevX.13.031007>.
- [20] Cody Jones. Improved accuracy for decoding surface codes with matching synthesis. *arXiv preprint arXiv:2408.12135*, 2024. URL <https://arxiv.org/abs/2408.12135>.
- [21] Xiangning Chen, Chen Liang, Da Huang, Esteban Real, Kaiyuan Wang, Yao Liu, Hieu Pham, Xuanyi Dong, Thang Luong, Cho-Jui Hsieh, et al. Symbolic discovery of optimization algorithms. In *Advances in Neural Information Processing Systems*, 2023. URL <https://arxiv.org/abs/2302.06675>.

- [22] Craig Gidney. Stim: a fast stabilizer circuit simulator. *Quantum*, 5:497, 2021. doi: 10.22331/q-2021-07-06-497. URL <https://doi.org/10.22331/q-2021-07-06-497>.
- [23] Google Quantum AI. Quantum error correction below the surface code threshold. *Nature*, 638:920–926, 2025. doi: 10.1038/s41586-024-08449-y. URL <https://doi.org/10.1038/s41586-024-08449-y>.